Hindawi
International Journal of Aerospace Engineering
Volume 2022, Article ID 3397763, 19 pages
https://doi.org/10.1155/2022/3397763

Research Article

Shock Boundary Layer Interaction and Aero-Optical Effects in a Transonic Flow over Hemisphere-on-Cylinder Turrets

Xiang Ren,[1] **Huahua Yu**,[1] **Xianghong Yao**,[2] **Hua Su**,[1] **and Peng Hu**[1]

[1]*Institute of Applied Physics and Computational Mathematics, Beijing 100094, China*
[2]*China Aerodynamics Research and Development Center, Mianyang, Sichuan 621000, China*

Correspondence should be addressed to Huahua Yu; yu_huahua@iapcm.ac.cn

Received 15 July 2022; Revised 2 November 2022; Accepted 3 November 2022; Published 17 November 2022

Academic Editor: Hongbing Ding

Copyright © 2022 Xiang Ren et al. This is an open access article distributed under the Creative Commons Attribution License, which permits unrestricted use, distribution, and reproduction in any medium, provided the original work is properly cited.

Hemisphere-on-cylinder turrets are the main airborne optical platform structure. However, an unsteady shock boundary layer interaction (SBLI) would act on flow separation and turbulent wake, which causes serious aero-optical effects with high spatial and temporal frequency characteristics. In this paper, the SBLI phenomenon of a hemisphere-on-cylinder turret is recorded in a wind tunnel at Ma = 0.7 using shadowing and Mach-Zehnder interferometer measurements. Its wavefront distortion is measured using the Shack-Hartmann measurement. The detached eddy simulation (DES) based on SST k-ω turbulence model and ray-tracing methods are used to reproduce the transonic flow and optical aberration. Experiments and simulations suggest that the SBLI causes the flow to separate earlier relative to a subsonic flow over the turret. The time-averaged root-mean-square of optical path difference (OPD) over the beam aperture is $0.56\,\lambda$~$0.59\,\lambda$ with λ as the wavelength, while the root-mean-square of the time-averaged OPD is about $0.45\,\lambda$. The local shock and wavefront distortion have dual peak frequencies at $\mathrm{St}_D = fD/U_\infty = 0.24$ and 0.34, different from the single-peak-frequency phenomenon of a subsonic flow over turrets. Fast model decomposition of wavefront can be performed by proper orthogonal decomposition (POD) of its Zernike coefficients. The first two modes contain the shock's reciprocating motion.

1. Introduction

Hemisphere-on-cylinder turrets are the main structure of airborne optical platforms due to their sizeable visual field. They are widely used in point-to-point communication links, optical target tracking, directed energy weapons, etc. However, the blunt-body shape interacts with the incoming flow to form a complex flow encompassing all turbulent features such as boundary layers, separated shear layers, vortex wake, necklace vortices, and other vortex structures. Depending on the flow structure formed by the different incoming velocities, the flow over a turret can be classified as subsonic (Ma < 0.55), transonic (0.55 < Ma < 1), and supersonic (Ma > 1) [1]. An unsteady shock boundary layer interaction (SBLI) acts on separated flow and turbulent wake in transonic flow and causes aero-optical effects with high spatial and temporal frequency characteristics. The aero-optical effects lead to adverse effects such as blurring, jittering, drifting, and light intensity reduction of the emitted beam or the received image [1, 2].

Optical aberrations are mainly quantified by optical path difference (OPD) caused by changes in refractive index due to nonuniform density fields, i.e., the refractive index integral over the path of a beam and removing its average value over the beam aperture.

Since the first Aero-Optics conference held in the USA in 1979 discussed the aerodynamic interference of airborne optical systems [3], the concept of aero-optical effects has been gradually formed and developed. Airborne laser turrets have been extensively studied, such as Airborne Laser (ABL), Advanced Tactical Laser (ATL), Airborne Aero-Optics Laboratory (AAOL), and AAOL-Transonic (AAOL-T) projects in the USA [4–6]. Literatures [1–3, 7–10] summarized the aero-optical effect experiment and modeling research of turret.

Since the 1980s, a series of wind tunnel experiments have been conducted in the USA to measure the properties of

laser propagation through air, quantify aerodynamic perturbations of distorted beams, and confirm the assumed relationship between aerodynamics and optics [3]. In the last decade, transient flow and optical aberration experiments were feasible with high time-bandwidth noncontact optical measurements, such as shadowing/striping, Mach-Zehnder interferometer, particle image velocimetry (PIV), and Shack-Hartmann wavefront measurement sensors in particular [11]. There are many wind tunnel experiments for flows over hemispherical and hemisphere-on-cylinder turrets and their aero-optic measurements [12–17]. Considering the differences between flight experiments and wind tunnel experiments, the AAOL and AAOL-T projects used two aircraft at subsonic and transonic speeds to measure the aero-optical performance of turrets [18, 19]. Figure 1 summaries some wind tunnel and flight experiments of subsonic/transonic flow over turrets and their incoming flow conditions, including Mach numbers and Reynolds numbers based on turret diameter (Ma and Re_D). The corresponding states for different turret diameters at sea level flight altitudes are indicated. These studies move from low speed to transonic flow and focus more on unsteady characteristics. On the other hand, experimental methods mainly obtain information on the superposition of the three-dimensional transient flow along the beam.

It can be directly estimated for subsonic flow using potential function analysis or a steady-state turbulence model. However, the aero-optical effects of large gradient shock boundary layer interference in transonic and supersonic flows are more complicated [1, 19]. Therefore, the high-precision numerical simulation analysis of the aero-optical effect of the laser turret requires an advanced transient simulation. Numerical simulations for aero-optics can be decoupled into two processes: flow simulation and optical transport simulation. The beam propagation in transient flow is directly calculated using ray tracing, simple integration of the refractive index field along the optical path for optical transport simulation. White [20] has validated this method by performing it in a supersonic turbulent boundary layer. However, for flow simulation, the direct numerical simulation (DNS) method, which can portray the minimum vortex (~ Kolmogorov scale), is impractical due to the high Reynolds number ($10^5 \sim 10^7$) characteristic, and the Reynolds-averaged N-S equation (RANS) method can only obtain time-averaged properties. The requirement for optical transport resolution proposed by Mani et al. and Mathews et al. [21, 22] provides a basis for the large eddy simulation (LES) method. Further considering the effect of the wall, researchers [15, 23–28] are trying hybrid RANS/LES methods such as detached eddy simulation (DES) and wall-modeled LES (WMLES) for the numerical simulation for the flow over laser turrets, shown as Table 1, but only with limited success at subsonic flow. However, the simulated statistical fluctuations differ from the experiments. There are also challenges to the simulation of SBLI in transonic flows [29].

In this paper, through wind tunnel experiments and numerical simulations, the fluid dynamics and aero-optical effects of transonic turrets are studied, especially the local shock and separation flow at the zenith of the turret. It is organized as follows: Section II introduces the hemisphere-on-cylinder turret's experimental conditions and measurement equipment. Section III describes the SST-DES and ray-tracing methods for fluid dynamics and optical transport simulation and presents several optical evaluation parameters. Section IV compares the experimental and simulated results of fluid dynamics and aero-optical effects in terms of time averages and temporal characteristics. Section V provides conclusions.

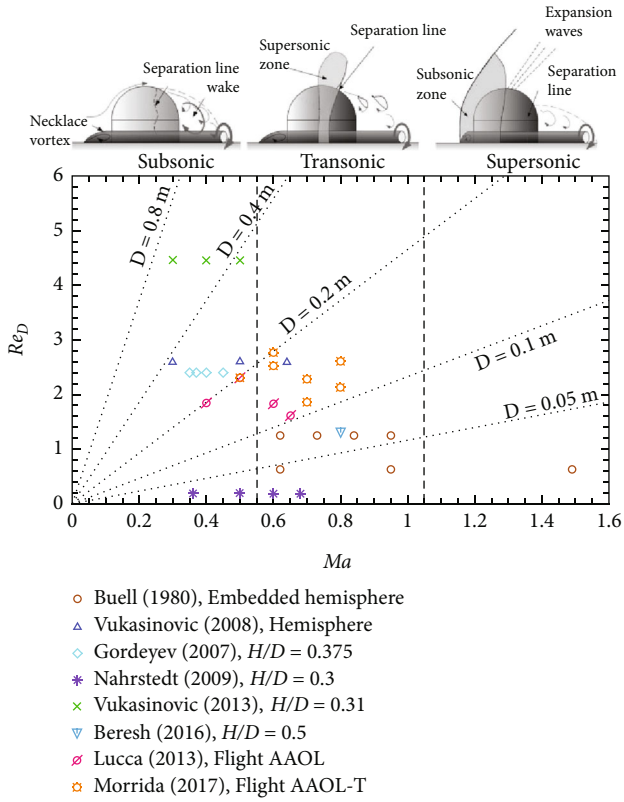

FIGURE 1: Some wind tunnel and flight experiments of subsonic/transonic flow over turrets and their incoming flow conditions, including Mach numbers and Reynolds numbers based on turret diameter.

2. Physical Model

Wind tunnel experiments on fluid dynamics and aero-optics of transonic flow over a hemisphere-on-cylinder turret with various freestream velocities (Ma = 0.3 ~ 0.7) have been performed. The experimental conditions and measuring instruments relevant to this study are described as follows.

A hemisphere-on-cylinder turret with a conformal window is shown in Figure 2. The diameter of the hemisphere is $D = 140$ m. The height of the cylinder is $H = D/2$, and the diameter of the conformal window is $D_l = 3/7\,D$. There is a laser beam with a wavelength of $\lambda = 532$ nm through the conformal window. The experiment was performed within a 0.6 m × 0.6 m transonic and supersonic wind tunnel facility of China Aerodynamics Research and Development Center (CARDC). The dried air with a stagnation pressure

Table 1: Some numerical simulations for flow over laser turrets.

Author	Turret size (m)	Ma	$Re_D \times 10^{-6}$	Numerical methods
Pond et al. [23]	3.2	0.76	51.5	k-ε RANS
Nahrstedt et al. [15]	0.3	0.4	2.9	k-ε RANS
Ladd et al. [24]	0.3	0.4	2.9	RANS, DES
Morgan et al. [25]	0.3	0.4	2.9	DES
Jelic et al. [26]	—	0.45/0.85	6.3/9.5	DES
Coirier et al. [27]	0.6	0.4~2.5	2.7~16.6	DES
Mathews et al. [28]	—	0.4	2.3	WMLES

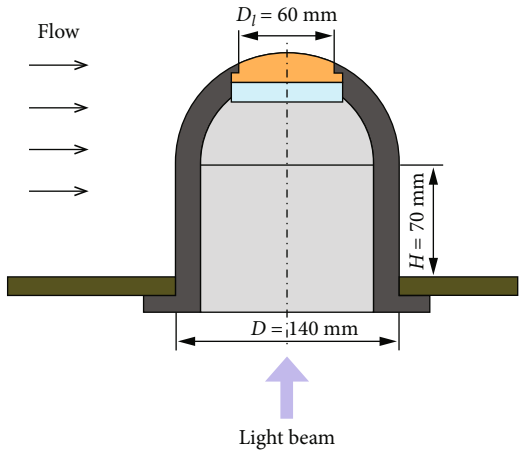

Figure 2: Hemisphere-on-cylinder turret model with a conformal window.

and temperature of 100 kPa and 288 K would reach a Mach number of Ma = 0.7 and a Reynolds number of $Re_D = 1.83 \times 10^6$ in the test section of the wind tunnel. Table 2 shows specific freestream flow parameters over the turret.

There are small holes along the turret centerline for connecting differential pressure gauges to measure wall pressures. The pressure-measurement system has a range of 15 psi (103.42 kPa), a sampling frequency of 50 kHz, and an accuracy of ±0.05%. The beam passing through the complex flow is recorded by high-speed, two-dimensional Shack-Hartmann wavefront measurement, and Mach-Zehnder interferometer measurement at the same time. Wavefront aberrations are expressed as a distribution of optical path difference (OPD). The high-speed Shack-Hartmann wavefront measurement was pioneered by Wyckham and Smits to measure aero-optical distortions since 2009 [30]. An expanded laser beam passes through the flow, and an array of lenslets focuses a grid of spots onto a digital camera, as shown in Figure 3. Each spot is projected onto a position normal to the local average wavefront slope across that lenslet. The wavefront slope is measured at a number of points, and the phase shape of the distorted wavefront is then reconstructed from the slopes [30, 31]. It can record wavefront with a spatial resolution of 23 × 23 subapertures at a framing rate of 20 kHz. The recording time is 1 s, or about 1623 D/U_∞. The Mach-Zehnder interferometer measurement can directly observe the flow field based on the interference between the disturbed beam and the original beam at 20 kHz. Figure 3 shows the experimental schematic and images for schlieren (Ma = 0.65), Mach-Zehnder interferometer, and Shack-Hartmann subaperture spots. Two individuals repeated wind tunnel experiments that were performed to verify the accuracy of the measurement data. In addition, a schlieren system, with its optical paths perpendicular to the turret axis and flow direction, records flow information at the zenith of the turret, especially the local shock and separation shear layers. The window diameter of the schlieren is 200 mm, the resolution is 896 × 896, the frame rate is 25 kHz, and the exposure time is 10 μs. It should be noted that the schlieren image in Figure 3(b) and the oil flow image below are from another experiment at Ma = 0.65. However, the flow structure is consistent with that of this paper.

Here, the pressure measurement can directly obtain the wall pressure distribution and verify with the results of the numerical simulation. Schlieren and Mach-Zehnder interferometer are used to observe the flow field at the zenith of the turret, and Shack-Hartmann is used to measure the optical distortion caused by this flow field.

Table 2: Freestream flow parameters.

Physical quantity	Symbol	Value	Unit
Mach number	Ma	0.7	—
Reynolds number	Re_D	1.83×10^6	—
Total temperature	T_t	288	K
Total pressure	p_t	100	kPa
Static temperature	T	262.30	K
Static pressure	p	72.093	Pa
Density	ρ	0.9575	Kg/m^3
Velocity	U	227.26	m/s

3. Numerical Method

The fluid dynamics and optical transmission are decoupled to simulate the aero-optical effect of the turret. The DES method based on SST k-ω turbulence model, namely, SST-DES, is used for fluid dynamics. In terms of optical transmission, a self-developed program that considers the influence of the density field is adopted. When simulating fluid dynamics, the density field is collected every 1×10^{-4} s, or $0.16D/U_\infty$ to calculate the wavefront of the beam.

3.1. Flow Simulation Method. The SST-DES model uses a switch function to convert the computational fluid dynamics

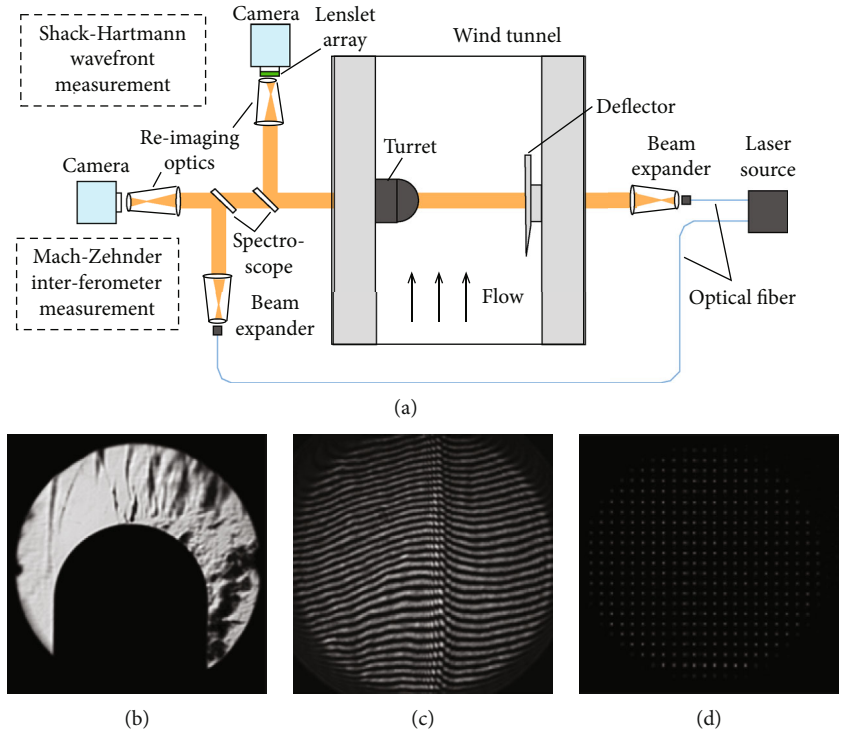

FIGURE 3: (a) Experimental schematic and images for (b) schlieren (Ma = 0.65), (c) Mach-Zehnder interferometer, and (d) Shack-Hartmann subaperture spots.

method between the SST k-ω RANS model and the large eddy simulation (LES). The SST k-ω RANS model can deal with the transport of turbulent shear stress in the inverse pressure gradient boundary layer, while the LES method can simulate the large-scale vortices that have a significant influence on optical transmission. Like SST k - ω RANS, the conservation equations of SST-DES include continuity, momentum, and energy conservation equations as well as turbulent kinetic energy k- and specific dissipation rate ω -equations [32]

$$\frac{\partial \rho}{\partial t} + \frac{\partial}{\partial x_j}\left(\rho u_j\right) = 0, \tag{1}$$

$$\frac{\partial}{\partial t}\left(\rho u_i\right) + \frac{\partial}{\partial x_j}\left(\rho u_i u_j\right) - \frac{\partial \sigma_{ij}}{\partial x_j} = -\frac{\partial p}{\partial x_i}, \tag{2}$$

$$\frac{\partial}{\partial t}\left(\rho h\right) + \frac{\partial}{\partial x_j}\left(\rho h u_j\right) + \frac{\partial q_j}{\partial x_j} = P_h + \frac{Dp}{Dt}, \tag{3}$$

$$\frac{\partial k}{\partial t} + \frac{\partial}{\partial x_j}\left(k u_j\right) - \frac{\partial}{\partial x_j}\left[\left(\nu + \frac{\nu_t}{\sigma_k}\right)\frac{\partial k}{\partial x_i}\right] = P_k - \beta^* k\omega F_{\mathrm{DES}}, \tag{4}$$

$$\frac{\partial \omega}{\partial t} + \frac{\partial}{\partial x_j}\left(\omega u_j\right) - \frac{\partial}{\partial x_j}\left[\left(\nu + \frac{\nu_t}{\sigma_\omega}\right)\frac{\partial \omega}{\partial x_i}\right] = P_\omega - \beta\omega^2 + 2(1 - F_1)\sigma_{\omega 2}\frac{1}{\omega}\frac{\partial k}{\partial x_j}\frac{\partial \omega}{\partial x_i}, \tag{5}$$

where t is the time, (x_1, x_2, and x_3) are Cartesian coordinates, u_i is the velocity component in the direction, x_i. ρ, p, T, k, and ω are the densities, kinematic pressure, temperature, turbulent kinetic energy, and specific dissipation rate, respectively, and $h = c_p T$ is the enthalpy. The state equation for an ideal gas, $p = \rho RT$, is used to close the conservation equations above. $\sigma_{ij} = \mu[((\partial u_i/\partial x_j) + (\partial u_j/\partial x_i)) - 2/3(\partial u_k/\partial x_k)\delta_{ij}]$ is the viscous stress tensor. $q_j = -\kappa\partial T/\partial x_j$ is the heat flux. The viscosity coefficient of air is taken as Sutherland Law, or $\mu = \mu_{\mathrm{ref}}(T/T_{\mathrm{ref}})^{3/2}(T_{\mathrm{ref}} + T_0)/(T + T_0)$ with $\mu_{\mathrm{ref}} = 1.716 \times 10^{-5}$ Ns/m^2, $T_{\mathrm{ref}} = 273$ K, and $T_0 = 110.4$ K. The thermal conductivity $\kappa = c_p\mu/\mathrm{Pr}$ with the constant pressure specific heat capacity $c_p = 1004.6$ J/kg/K and Prandtl number Pr = 0.71.

The production terms in energy, k-, and ω-equations are evaluated as [32]

$$P_h = \nu_t\left(\frac{\partial u_i}{\partial x_j} + \frac{\partial u_j}{\partial x_i}\right)\frac{\partial u_i}{\partial x_j}, \tag{6}$$

$$P_k = \min\left\{P_h, c_1\beta^* k\omega\right\}, \tag{7}$$

$$P_\omega = \alpha\Omega^2, \tag{8}$$

where $\Omega = \sqrt{2s_{ij}s_{ij}}$ denotes the invariant measure of the strain rate, and $s_{ij} = 1/2((\partial u_i/\partial x_j) + (\partial u_j/\partial x_i))$ is the strain rate tensor. The turbulence viscosity ν_t is obtained using

$$\nu_t = \frac{k}{\max\left(\omega, \Omega F_2/a_1\right)}, \tag{9}$$

where F_2 is a blending function to ensure that the Johnson-King model only can be active in the boundary layer, and it is defined as

$$F_2 = \tanh\left(\gamma^2\right), \gamma = \max\left(2\frac{\sqrt{k}}{\beta^*\omega y}, \frac{500\nu}{y^2\omega}\right), \quad (10)$$

where y is the distance to the wall.

F_1 in Equation (1) is another blending function to switch the SST model between the k-ω and k-ε formulation

$$F_1 = \tanh\left(\xi^4\right), \xi = \min\left[\max\left(\frac{\sqrt{k}}{\beta^*\omega y}, \frac{500\nu}{y^2\omega}\right), \frac{4\sigma_{\omega 2}k}{CD_\omega y^2}\right], \quad (11)$$

where

$$\mathrm{CD}_\omega = \max\left(2\sigma_{\omega 2}\frac{1}{\omega}\frac{\partial k}{\partial x_i}\frac{\partial \omega}{\partial x_i}, 10^{-10}\right). \quad (12)$$

The constants α, β, σ_k, and σ_ω are blended between the two formulation

$$\varphi = F_1\varphi_1 + (1 - F_1)\varphi_2, \quad (13)$$

where the values of the constants for the two formulations are

$$k-\omega : \alpha_1 = \frac{5}{9}, \beta_1 = \frac{3}{40}, \sigma_{k1} = 0.85, \sigma_{\omega 1} = 0.5, \quad (14)$$

$$k-\varepsilon : \alpha_2 = 0.44, \beta_2 = 0.0828, \sigma_{k2} = 1, \sigma_{\omega 2} = 0.856, \quad (15)$$

and other constants are

$$\beta^* = 0.09, a_1 = 0.31, c_1 = 10. \quad (16)$$

The switching function F_{DES} incorporates DES features into Equation (1).

$$F_{\mathrm{DES}} = \max\left[(1 - F_2)\frac{L_{\mathrm{RANS}}}{C_{\mathrm{DES}}\Delta}, 1\right], \quad (17)$$

where the turbulent length scale is $L_{\mathrm{RANS}} = \sqrt{k}/\beta^*\omega$. The grid scale Δ is set as the cube root of cell volume and $C_{\mathrm{DES}} = 0.61$. Note that when $F_{\mathrm{DES}} = 1$, Equation (1) degenerates to the standard SST k-ω RANS model. F_2 is added to reduce the dependence of SST-DES on the grid resolution.

Spalding's law is used on the surface of the turret to match the laminar sublayer and the log-law [33]

$$y^+ = u^+ + e^{-\kappa B}\left[e^{\kappa u^+} - 1 - \kappa u^+ - \frac{1}{2}\left(\kappa u^+\right)^2 - \frac{1}{6}\left(\kappa u^+\right)^3\right] \quad (18)$$

where $u^+ = u/u_\tau$ is the normalized velocity with the friction velocity $u_\tau = \sqrt{\tau_w}$, and the wall shear stress τ_w. $y^+ = yu_\tau/\nu$ is the normalized distance to the wall with the kinematic viscosity ν. The model parameters have values $\kappa = 0.4$ and $B = 5.5$.

A transient solver for the turbulent flow of compressible fluids in OpenFOAM, rhoPimpleFoam is used for the SST-DES model. OpenFOAM is an open-source C++, CFD program that uses a finite volume approach and supports parallel computing. Its rhoPimpleFoam solver couples the PISO and SIMPLE algorithms, thus supporting convergence when CFL > 1. In this paper, the time step in the stabilization phase is set to $3 \times 10^{-3}\, D/U_\infty$, and the corresponding global maximum CFL does not exceed 4. The gradient terms in Equation (1) adopt the second-order center format, the divergence terms adopt the upwind–convective format, and the time terms adopt the first-order implicit format. The SST RANS model was used to obtain the quasi-steady flow, and then the SST-DES model was changed to perform transient simulation. The total computation time is/about $1600\, D/U_\infty$. The flow field is saved every 1×10^{-4} s $(0.05\, D/U_\infty)$ for subsequent optical transmission analysis during this period.

The stable freestream flow would form a complex wake behind the turret, a computational domain consisting of a quarter sphere and a half cylinder is shown in Figure 4. To avoid the influence of far-field boundaries, the diameter of the quarter sphere is 30 D, and the length of the half cylinder is 30 D. Hexahedral meshes are used, shown as the partial enlargement in Figure 4(a). The mesh size along the cylindrical surface is smaller than 0.0071 D, and the height of the first layer of meshes is 0.0014 D, thus ensuring $y^+ < 100$. There are 10.6 million cells. To ensure mesh independence, multiple sets of meshes have been aligned based on the time-averaged pressure distribution on the turret surface.

The inlet and outlet boundary conditions are set according to the freestream flow parameters in Table 2. The pressure condition at the outlet is set as a wave transmissivity boundary to avoid the influence of outflow. The cylindrical surfaces and the bottom plate are set as no-slip and adiabatic walls. It has shown that whether the wall is set to adiabatic or constant temperature has a negligible effect on the flow. Furthermore, as the boundary layer on the bottom plate is very thin relative to the turret's height, this boundary layer has no effect on the flow around the turret hemisphere, so the grid near the bottom plate is not separately encrypted.

3.2. Optical Transmission Method. The Gladstone-Dale relation is utilized to simulate transient wavefront snapshots in unsteady density fields. It is a linear relationship between

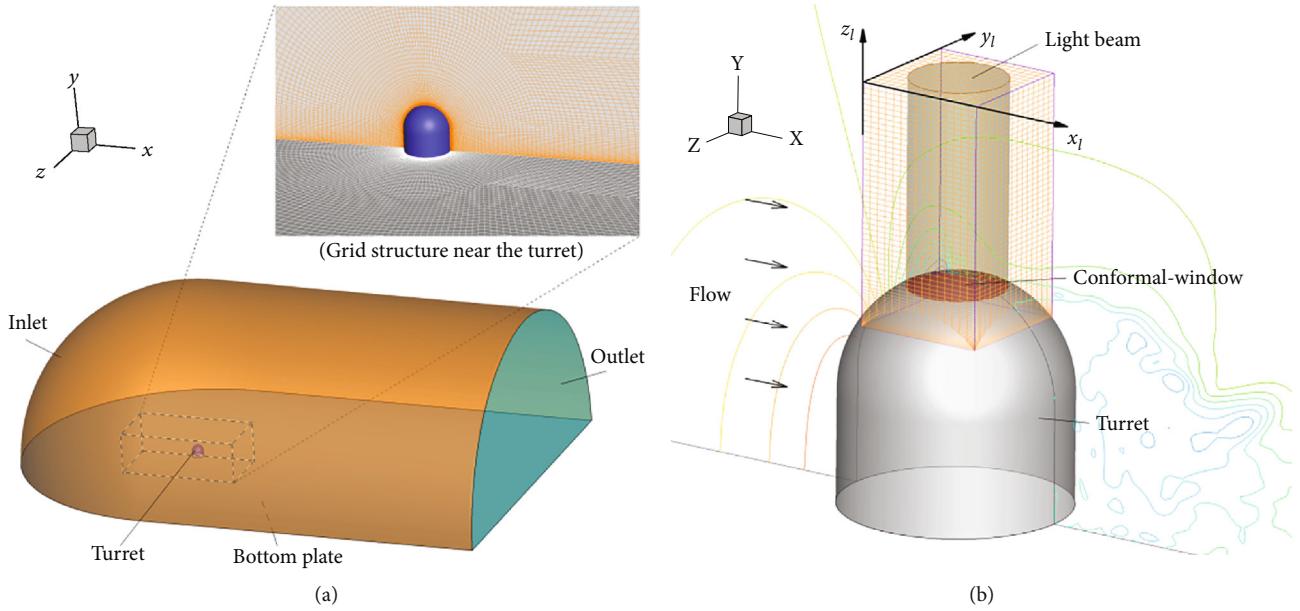

FIGURE 4: Computational domain and mesh for simulation: (a) fluid and (b) optical.

the air's index of refraction n and the density ρ

$$n = 1 + K_{\mathrm{GD}}\rho, \tag{19}$$

where K_{GD} is the Gladstone-Dale constant, and it depends on the gas mixture and the laser wavelength λ [34]. Here, for air over the visible-to-IR wavelength range, $K_{\mathrm{GD}} = (1 + 7.52 \times 10^{-15}/\lambda^2) \times 2.23 \times 10^{-4}$ with the unit of λ is m.

The wavefront distortion is usually quantified by the optical path difference (OPD), defined as the conjugate of the wavefront' displacement from the mean wavefront over the beam's aperture. For a compact aberration field near the turret, the OPD can be simplified to integrate the index of refraction along paths parallel to the propagation direction and remove the mean of these integrated values over the aperture [2, 7]. The integration is the optical path length (OPL). For the coordinate $O\text{-}x_l y_l z_l$ showed in Figure 4(b),

$$\mathrm{OPD}(x_l, y_l, t) = \mathrm{OPL}(x_l, y_l, t) - \int_S \mathrm{OPL}(x_l, y_l, t)\mathrm{d}x_l\mathrm{d}y_l, \tag{20}$$

with

$$\mathrm{OPL}(x_l, y_l, t) = \int_{z_{l,1}}^{z_{l,2}} n(x_l, y_l, z_l, t)\mathrm{d}z_l, \tag{21}$$

where S is the face of the aperture, and $z_{l,1}$ and $z_{l,2}$ are the positions of wavefront's emission and reception, respectively. Note that some use the conjugate of the OPD to represent the optical wavefront, $\mathrm{W}(x_l, y_l, t) = -\mathrm{OPD}(x_l, y_l, t)$.

Here, an independent program is utilized to calculate the OPD of the laser beam aberrated by the snapshots of the turbulent field multiple times. A Cartesian optical grid that can wrap the aperture is used, and the density field is interpolated from the grid structure shown in Figure 4(a). There is steady lensing, unsteady tilt or beam jitter, and high-order distortion effects in OPD [1]. This decomposition is useful when correcting wavefront aberrations in adaptive optics, where the steady-state lens term is corrected by a large range-of-motion deformation mirror, the tilt/jitter component can be removed using a fast steering mirror, and the high-order distortion terms can be compensated for by using a high bandwidth deformation mirror [35]. Large-scale eddies (larger than the optical aperture) cause beam tilt/jitter, while small-scale eddies (smaller than the optical aperture) cause high-order distortion such as optical scattering, beam spread, and consequent attenuation of intensity [36].

Beam-jitter effects are removed by adding a spatial skew factor $(A(t)x_l + B(t)y_l)$ when computing $\mathrm{OPD}(x_l, y_l, t)$, where $A(t)$ and $B(t)$ are determined using the least-squares method on $\mathrm{OPD}(x_l, y_l, t)$. It is clear to analyze high-order distortions that characterize the effect of subaperture scale turbulence on the shape and intensity of the beam phase distortion.

In addition, the root-mean-square of $\mathrm{OPD}(x_l, y_l, t)$ can be used to characterize transient OPD fluctuations,

$$\mathrm{OPD}_{\mathrm{rms}}(t) = \sqrt{\frac{1}{S}\int_S \mathrm{OPD}^2(x_l, y_l, t)\mathrm{d}x_l\mathrm{d}y_l}. \tag{22}$$

And the time average of $\mathrm{OPD}(x_l, y_l, t)$ is recorded as $\langle \mathrm{OPD}(x_l, y_l)\rangle$, which represents the steady-lensing effect caused by the time-averaged density nonuniformity. The time average of $\mathrm{OPD}_{\mathrm{rms}}(t)$ is recorded as $\langle \mathrm{OPD}_{\mathrm{rms}}\rangle$.

Proper orthogonal decomposition (POD) [37, 38] is used to extract the main modes of the wavefront. POD characterizes $\mathrm{OPD}(x_l, y_l, t)$ as the sum of the product of the

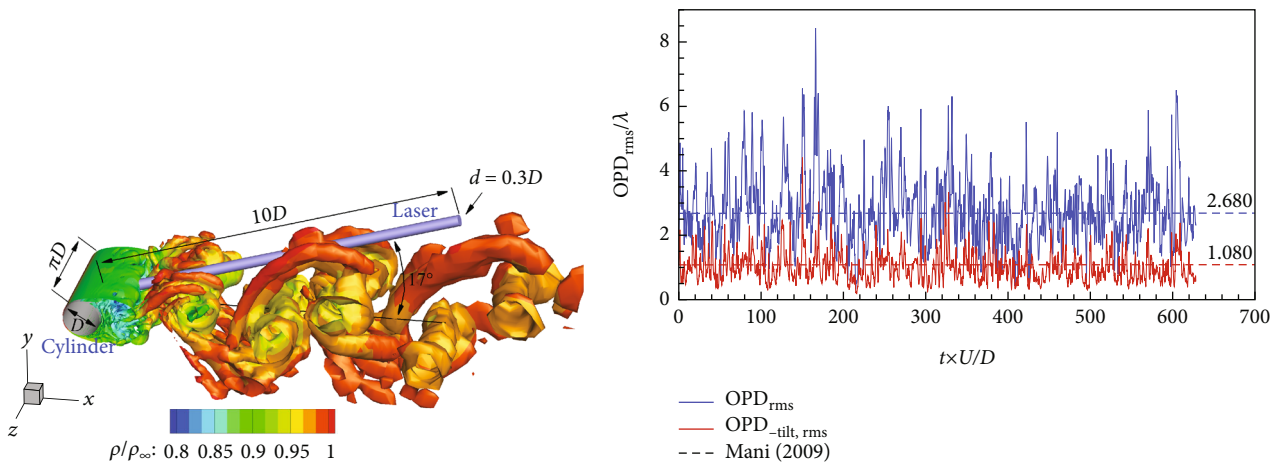

Figure 5: (a) The separated shear layer and the wake behind the cylinder, and (b) beam wavefront distortion.

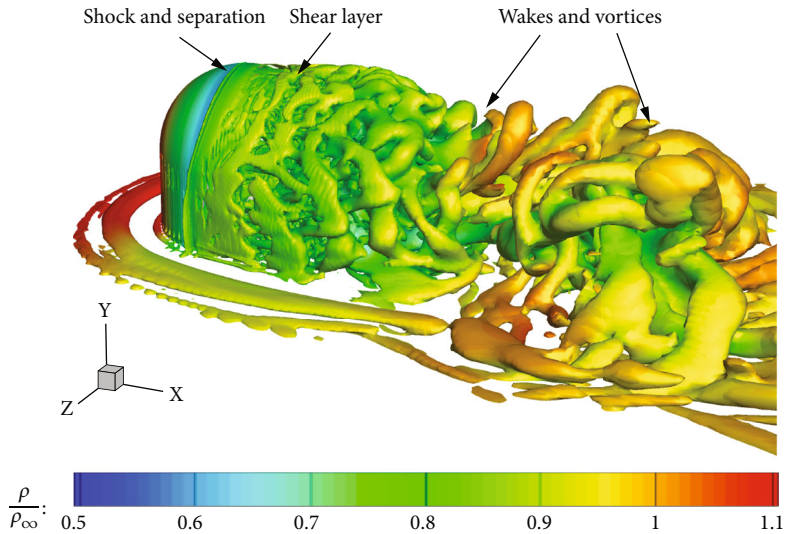

Figure 6: Transonic flowfield structure over a turret (isosurface: $Q = 0.05U_\infty^2/D^2$).

orthogonal space basis $\Phi_n(x_l, y_l)$ and the corresponding time coefficient $a_n(t)$

$$\mathrm{OPD}(x_l, y_l, t) = \sum_k a_k(t)\Phi_k(x_l, y_l). \tag{23}$$

In this paper, Zernike polynomials are used to fit the wavefront first, and then POD decomposition of the Zernike coefficients is performed.

The Zernike polynomials are a sequence of continuous and orthogonal polynomials over a unit circle. Zernike polynomials have the least information redundancy in describing the wavefront, and its various order modes correspond to the Seidel aberration coefficients in optics. Therefore, it is widely used for the reconstruction of circular wavefront [39]. The function describing an arbitrary wavefront in polar coordinates $(r\cos\theta, r\sin\theta) = ((2x_l/D_l), (2y_l/D_l))$ is

$$\mathrm{OPD}(x_l, y_l, t) = \sum_{j=0}^{J} C_j(t)Z_n^m(r, \theta), \tag{24}$$

where the radial order is $n = \mathrm{roundup}\{[-3 + (9 + 8j)^{1/2}]/2\}$, and the angular frequency is $m = 2j - n(n+2)$. $C_n^m(t)$ is the Zernike coefficients, and $Z_n^m(r, \theta)$ is the polynomials

$$\begin{aligned} Z_n^m(r, \theta) &= R_n^m(r)\cos(m\theta) \quad \text{for } m \geq 0 \\ Z_n^m(r, \theta) &= R_n^{-m}(r)\sin(-m\theta) \text{ for } m < 0 \end{aligned}, \tag{25}$$

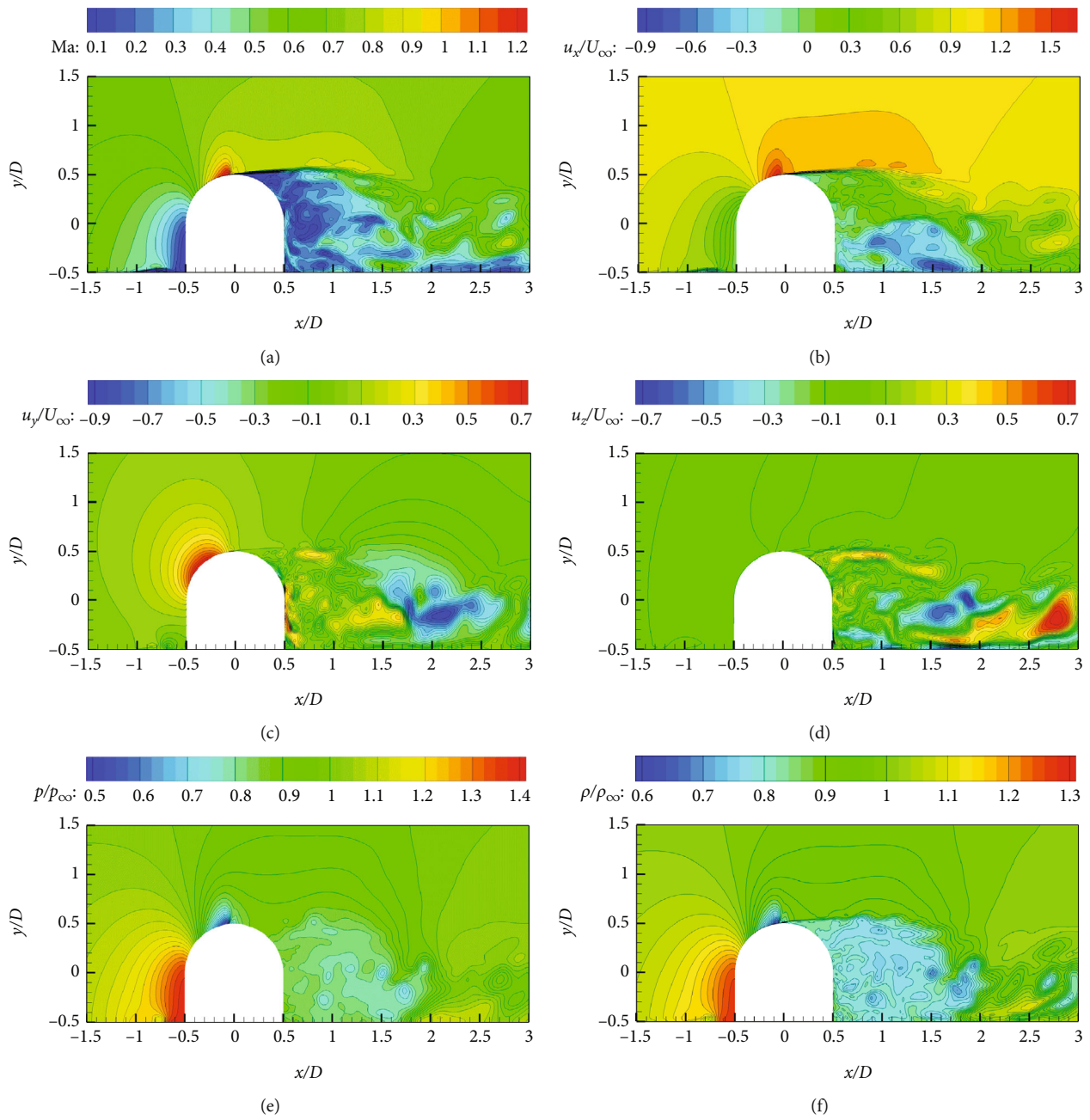

FIGURE 7: Transient flow snapshot along the turret centerline ($z = 0$): (a) Mach number, (b) streamwise velocity, (c) vertical velocity, (d) spanwise velocity, (e) static pressure, and (f) density.

with

$$R_n^m(r) = \sum_{l=0}^{n-m/2} \frac{(-1)^l (n-l)!}{l![1/2(n+m)-l]![1/2(n-m)-l]!} r^{n-2l}. \quad (26)$$

Note that since the piston and tip/tilt components are removed from each wavefront, the piston and tip/tilt modes in Zernike polynomial could be ignored.

$C_j(t)$ is decomposed using the one-dimensional POD technique based on singular value decomposition (SVD) [37], $C_j(t) = \sum_{k=0}^{J} a_k(t)\phi_k(j)$. Now the POD mode of OPD(x_l, y_l, t) is

$$\Phi_k(x_l, y_l) = \sum_{j=0}^{J} \phi_k(j) Z_n^m(r, \theta). \quad (27)$$

3.2.1. Validation of Fluid Simulation and Optical Transmission Methods. A flow over a circular cylinder [40] at $\mathrm{Re}_D = 3900$ and $\mathrm{Ma} = 0.4$ has been considered to validate the CFD method and wavefront transport method used in this

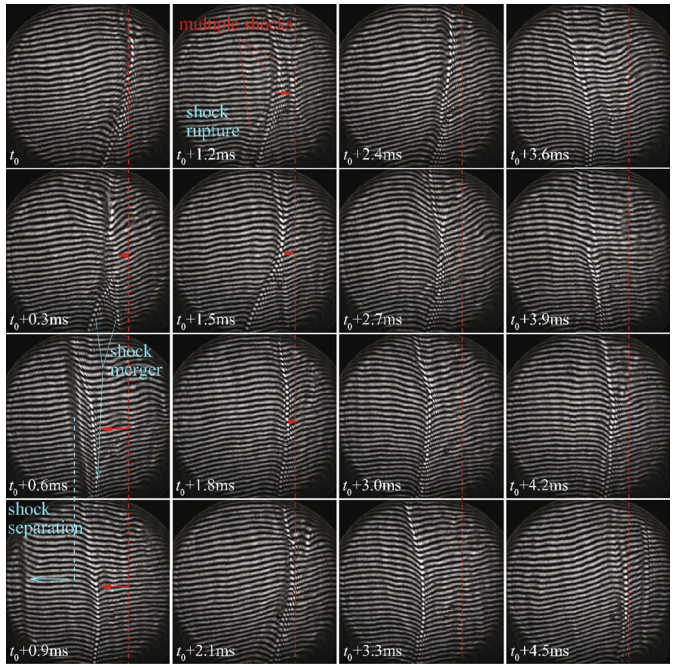

Figure 8: Mach-Zehnder images of the local shock from the vertical view (Ma = 0.7).

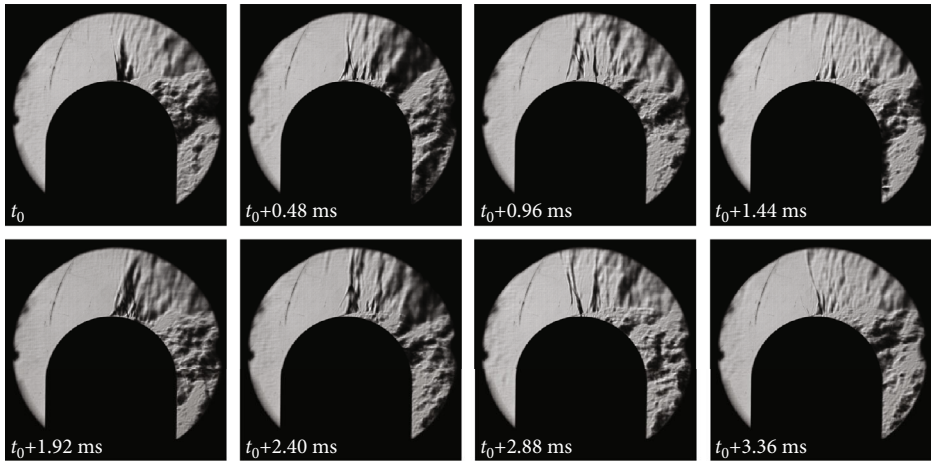

Figure 9: Schlieren images of the local shock from the side view (Ma = 0.65).

manuscript. Figure 5(a) shows the separated shear layer and the wake behind the cylinder obtained by our CFD method. The wavefront distortion of a beam passing through this complex flow is also reproduced using our wavefront propagation code, as shown in Figure 5(b). The time-averaged $\mathrm{OPD}_{\mathrm{rms}}$ and $\mathrm{OPD}_{-\mathrm{tilt,\,rms}}$ is 2.819 λ and 1.040 λ, which are within 5% of 2.680 λ and 1.080 λ in the literature.

4. Results and Discussion

4.1. Fluid Dynamics. It is a complex three-dimensional transonic flow over a hemisphere-on-cylinder turret. Figure 6 shows a transient vortex structure based on the Q-criterion and colored by the density field distribution. Here, the Q-criterion based on incompressible flow can illustrate some information.

The curved surface of the turret accelerates the subsonic freestream flow to supersonic speed and forms a local shock. The local shock extends to the wall boundary layer of the turret, and the backpressure gradient of the shock causes the boundary layer to separate. The flow forms a separated shear layer behind the separation line and develops a wake composed of many vortices. In addition, there is a necklace vortex surrounding the turret on the bottom plate.

To better display the local shock, the separated shear layer, and the wake, Figure 7 shows flowfield snapshots along the turret centerline ($z = 0$), including Mach number, three velocity components, static pressure, and density, whose are dimensionless by freestream parameters. There is an apparent local

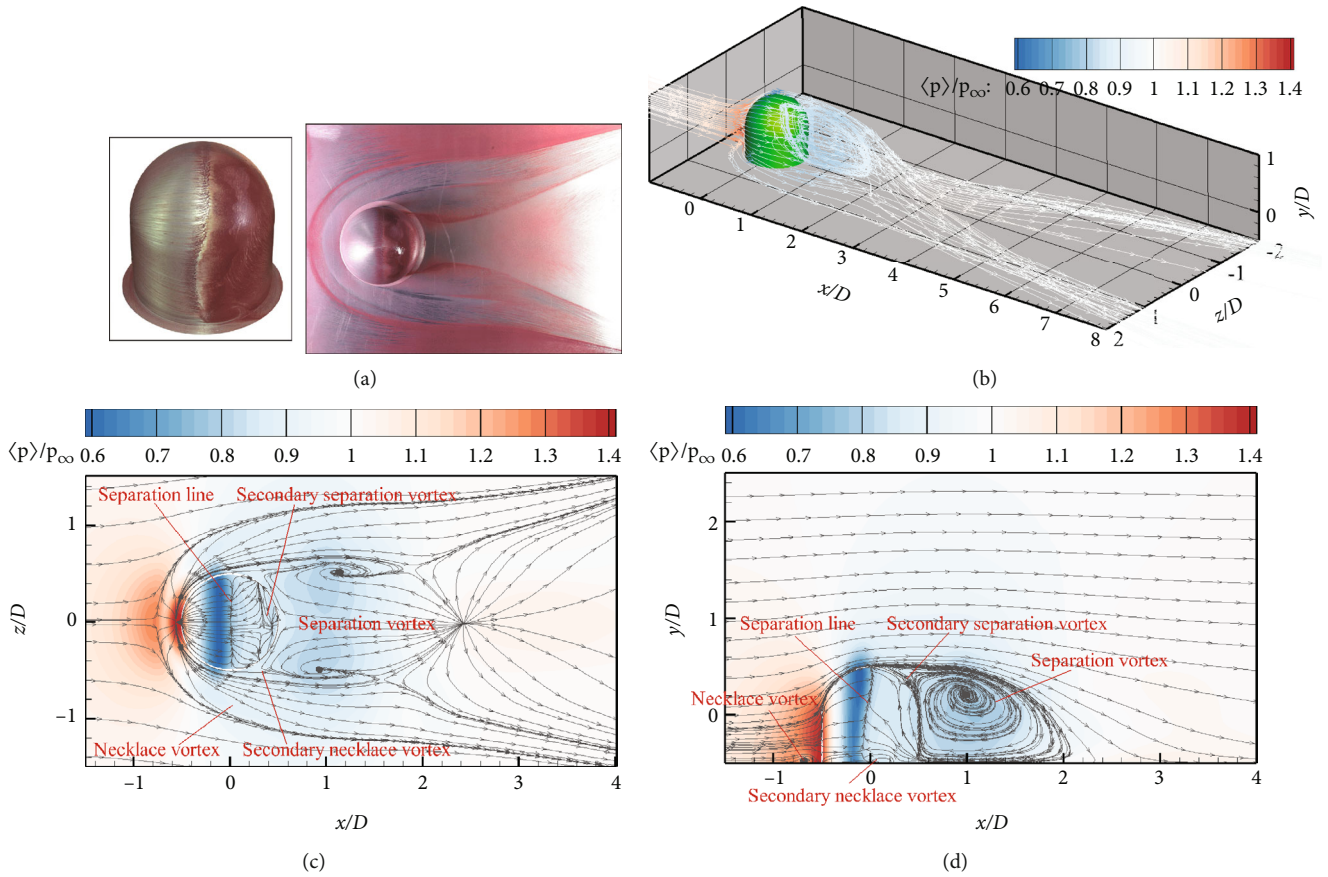

FIGURE 10: (a) Oil flow experiment (Ma = 0.65) and streamline distribution based on time-averaged velocity: (b) streamlines in 3D space, (c) streamline mapping near the bottom plate ($y = -0.5\,D$), and (d) streamlines along the turret centerline ($z = 0$).

shock at the zenith of the turret and a turbulent wake behind the turret. The sizeable adverse pressure gradient of the shock induces the flow separation of the boundary layer. The maximum fluctuations of the vertical and spanwise velocities in the wake are in the same order as the freestream velocity. There is a local shock moving back and forth on the surface of the turret, which is coupled to the period of the wake.

Figure 8 shows Mach-Zehnder images of the local shock and separated shear layers from the vertical view (Ma = 0.7). Figure 9 shows schlieren images of the local shock and separated shear layer from the side view (Ma = 0.65). The time interval of each frame in Figure 8 is 0.3 ms or about $0.5\,D/U_\infty$. The distinctive shading in Figure 8 represents the shock. Both experiments and simulations demonstrate the reciprocating motion of the local shock. In the first four frames, it moves forward, then in the next four frames, it moves backward, and the final eight frames show the backward and forward motion once again. So the period of shock motion is roughly 2.4 ms, or $4\,D/U_\infty$. Compared with one moving shock in numerical simulation, there are actually multiple shocks interacting at the zenith of the turret. Figure 8 shows the shock motion is accompanied by the separation, merging, breaking, and regeneration of shock waves. Many small discontinuous fringes follow the strong discontinuous fringes, and the moving multiple shocks and separation shear layers can be observed more clearly in Figure 9.

For the subsonic flow over a turret, there are mainly regular large-scale vortices behind the turret, and the transient flow snapshot can reflect the flow law in the separation zone of the turret. However, for the flow field snapshot of the transonic flow in this paper, the flow in the separation zone is "chaotic". Therefore, it is necessary to observe the law through the time-averaged flow field, as shown in Figure 10. Figure 10(a) is the experimental result of oil flow on the turret and bottom plate at Ma = 0.65. Figure 10(b) is the three-dimensional streamline of the time-averaged velocity colored by the dimensionless static pressure, and Figures 10(c) and 10(d) are streamlines closed to the bottom surface ($y = -0.5\,D$) and along the turret centerline ($z = 0$). Note that the freestream velocity of the oil experiment is slightly different from the simulation in this paper. Gordeyev et al. and Mathews [14, 41] have given the experimental and simulated streamlines on the bottom surface for subsonic flow over a turret (Ma = 0.35). The same colormap is used herein to pay tribute to them. In Figure 10, the necklace vortex, secondary necklace vortex, separation line, separation vortex, and secondary separation vortex can be distinguished, which are roughly the same structures as those in subsonic

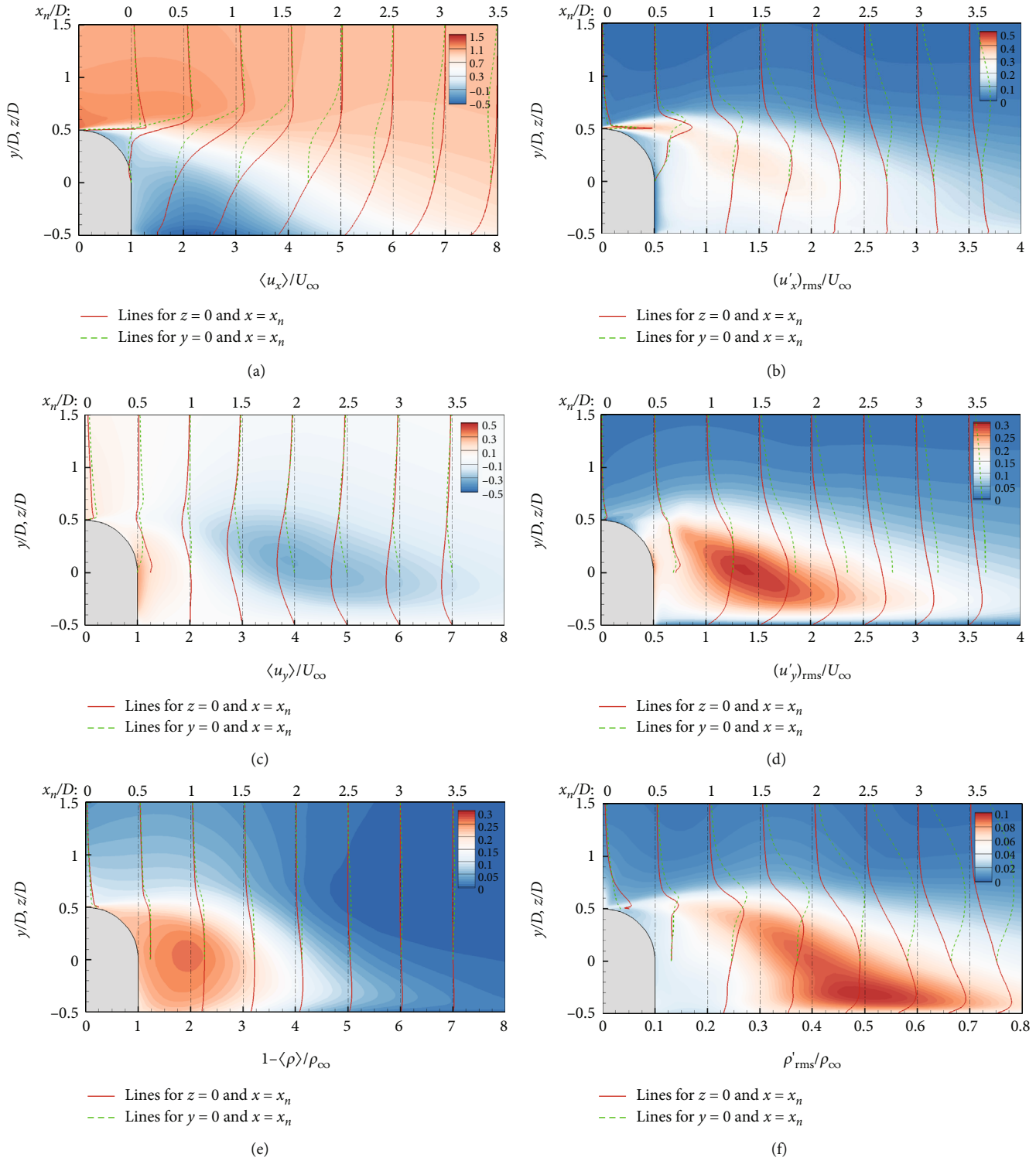

FIGURE 11: Time-averaged and fluctuation profiles of streamwise velocity, spanwise velocity, and density behind the turret, and it is colored by correlation quantities along the turret centerline ($z = 0$): (a, b) streamwise velocity, (c, d) spanwise velocity, and (e, f) density, where the solid red lines represent profiles along the turret centerline ($z = 0$), and the dashed green lines represent profiles on the horizontal plane ($y = 0$).

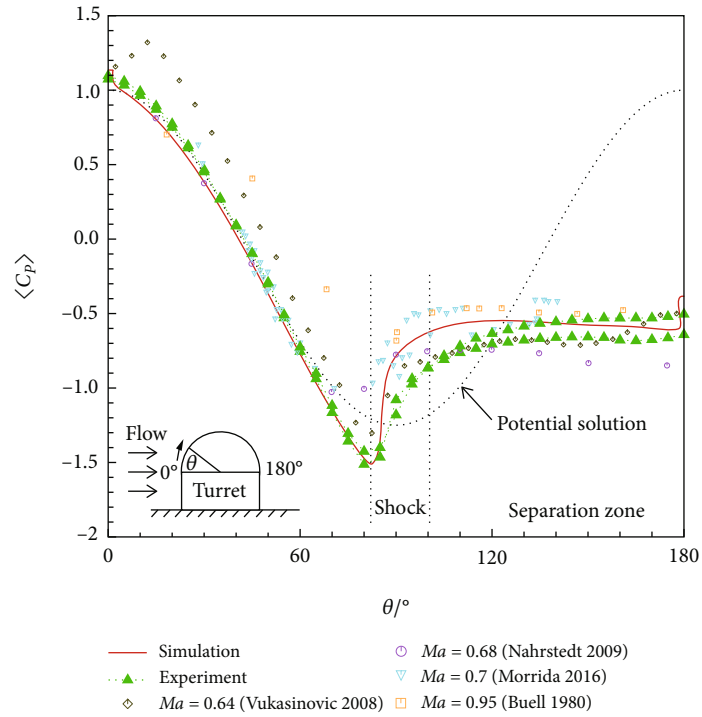

FIGURE 12: Time-averaged pressure coefficient distribution along the turret centerline obtained by the simulation and two experiments, where the solid red line represents numerical simulation, the green triangles represent two experiments, and hollow shapes represent data [12, 13, 15, 42].

flow, except for the "horn" vortex. The position of the time-averaged separation line in this study is different from that of the subsonic flow, where the local shock causes the separation. Figure 10(b) shows that the time-averaged separation line on the hemispherical surface of the turret is at $x = 0$, the separation line on the cylindrical surface moves forward slightly, and the separation line near the bottom plate returns to $x = 0$.

Figure 11 shows time-averaged and fluctuation profiles of streamwise velocity, spanwise velocity, and density behind the turret, containing information about the shear layer and wake. These figures are colored by correlation quantities along the turret centerline ($z = 0$). The solid red lines represent profiles at $x/D =$ along the turret centerline ($z = 0$), while the green dashed lines represent profiles at $x/D =$ on the horizontal plane ($y = 0$). The streamwise velocity fluctuation at the zenith of the turret is the largest, whose value is about $0.5\,U_\infty$. The streamwise and spanwise velocity fluctuations in the wake are roughly equivalent to the freestream velocity (about $0.1 \sim 0.4\,U_\infty$). Comparing the profiles along the turret centerline ($z = 0$) and on the horizontal plane $y = 0$, the wake behind the turret shows a short and fat development. Wang et al. [2] pointed out that the aero-optical effect is mainly composed of the steady-lensing term and the tilt/jitter term, and different methods are used to correct them. The time-averaged and fluctuations of the density, which determine the above two terms, are given in Figures 11(e) and 11(f). The minimum value of the time-averaged density at the zenith of the turret is about $0.8\,\rho_\infty$, and its fluctuation is about $0.05\,\rho_\infty$. The maximum fluctuation in the wake is about $0.1\,\rho_\infty$.

Figure 12 shows the time-averaged pressure coefficient distribution along the turret centerline obtained by two individual experiments and a numerical simulation. It is dimensionless by freestream parameters ($C_p = 2(p - p_\infty)/(\rho_\infty U_\infty^2)$). Figure 12 also shows the experimental data of Buell, Vukasinovic et al., Nahrstedt et al., and Morrida et al. [12, 13, 15, 42]. The theoretical potential solution curve ($C_p(\theta) = 1 - (9/4)\sin^2\theta$) for the incompressible inviscid flow over a sphere is also drawn in Figure 12.

It shows the following results:

(i) The pressure is maximum at the stagnation point of the turret, $C_{p,0} \approx 1.1$ and gradually decreases on the windward side ($\theta > 80\circ$). Since the shock oscillates in the range $80\circ < \theta < 100\circ$, the pressure here rises rapidly due to the local shock. In the flow separation region ($\theta > 100\circ$), the pressure is stable between $C_P = -0.5 \sim -0.8$

(ii) In the windward region ($\theta > 80\circ$), the experimental and simulation results agree with the potential function curve and the hemisphere-on-cylinder turret data of Buell, Nahrstedt et al., and Morrida et al. [12, 15, 42]. It demonstrates the validity of our

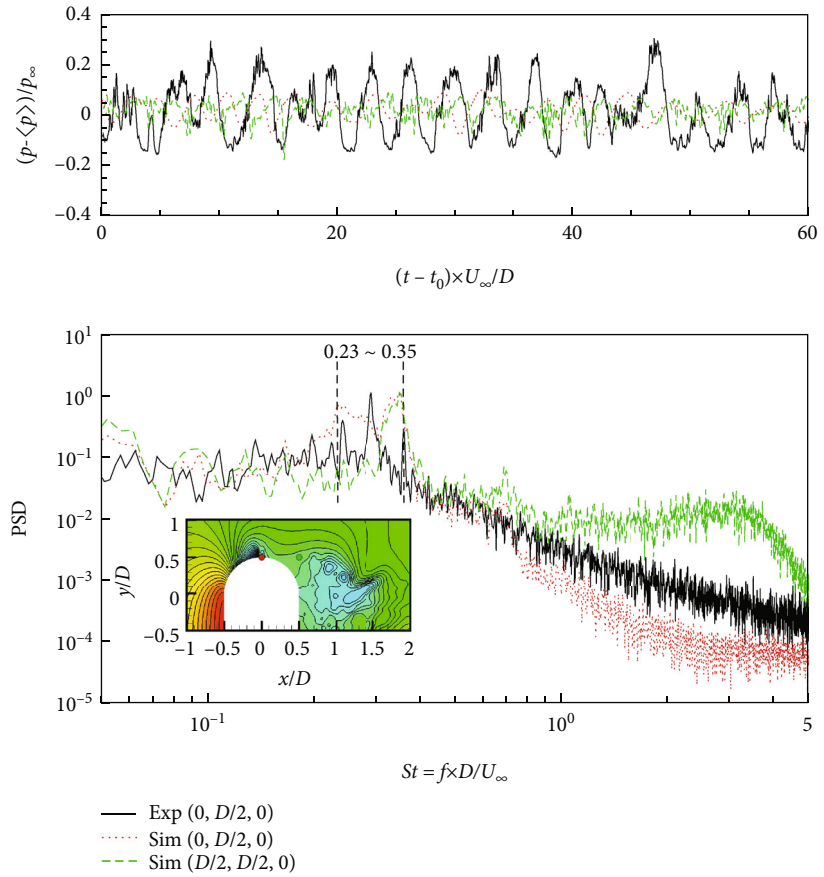

FIGURE 13: Transient pressures and their power spectral density (PSD), where the solid black line represents $(0, D/2, 0)$ for experiment, and the red dotted line and green dotted line represent $(0, D/2, 0)$ and $(0, D/2, D/2)$ for simulation.

experiments and data. It should be emphasized that the experiment of Vukasinovic et al. [13] adopts a pure hemispherical model, and the pressure stagnation point is in front of the hemisphere to approximately 15°. Since the boundary layer on the bottom plate always creates a necklace vortex at the base of the protrusion and changes the pressure distribution on the hemisphere, as shown in Figure 10(d), this shows that the hemisphere-on-cylinder turret can avoid the influence of the wall boundary layer and necklace vortex

(iii) In the shock and separation regions $(\theta > 80\circ)$, there are differences between each experimental data, which may be caused by different Reynolds and Mach numbers of the free stream. However, the minimum pressures obtained by the simulation and experiment are the same. The pressure coefficient error in the separation region is less than 0.2, which confirms that the experiment and the simulation are convincing. It should be noted that the transonic flow here is different from the subsonic flow (Ma < 0.55) of Gordeyev et al. and Vukasinovic et al. [43, 44], that is, the local shock mainly determines the separation position not only depends on the Reynolds number of the free stream, and the pressure recovery is faster. However, considering the forward and backward motion of the shock, the time-average pressure recovery has a gradient rather than a strong discontinuity

This study monitors the pressures at the local shock and the separated shear layer, or $p - \langle p\rangle/p_\infty$ at $(0,0.5D, 0)$ and $(0.5D, 0.5D, 0)$, and their power spectral density (PSD) are obtained by the fast Fourier transform (FFT) method for experiment and simulation, as shown in Figure 13. Here, the Strouhal number denotes dimensionless frequency, $St_D = fD/U_\infty$. Their time averages have been subtracted just to compare the periodic variations, and their power spectra are divided by their respective maximum values. The time-averaged pressures at the zenith of the turret for the simulation and two experiments are $0.717\,p_\infty$, $0.595\,p_\infty$, and $0.630\,p_\infty$. The time-averaged pressures at $(0.5D, 0.5D, 0)$ for simulation is $0.835\,p_\infty$. The pressure at the zenith of the turret has multiple frequencies in the range of $St_D = 0.23 \sim 0.35$ for experiment and simulation. Morrida et al. also observed the same two-frequency phenomenon in the Ma = 0.7 flow over a turret [19, 45]. Note that this is different from the subsonic flow over a turret. For a subsonic flow,

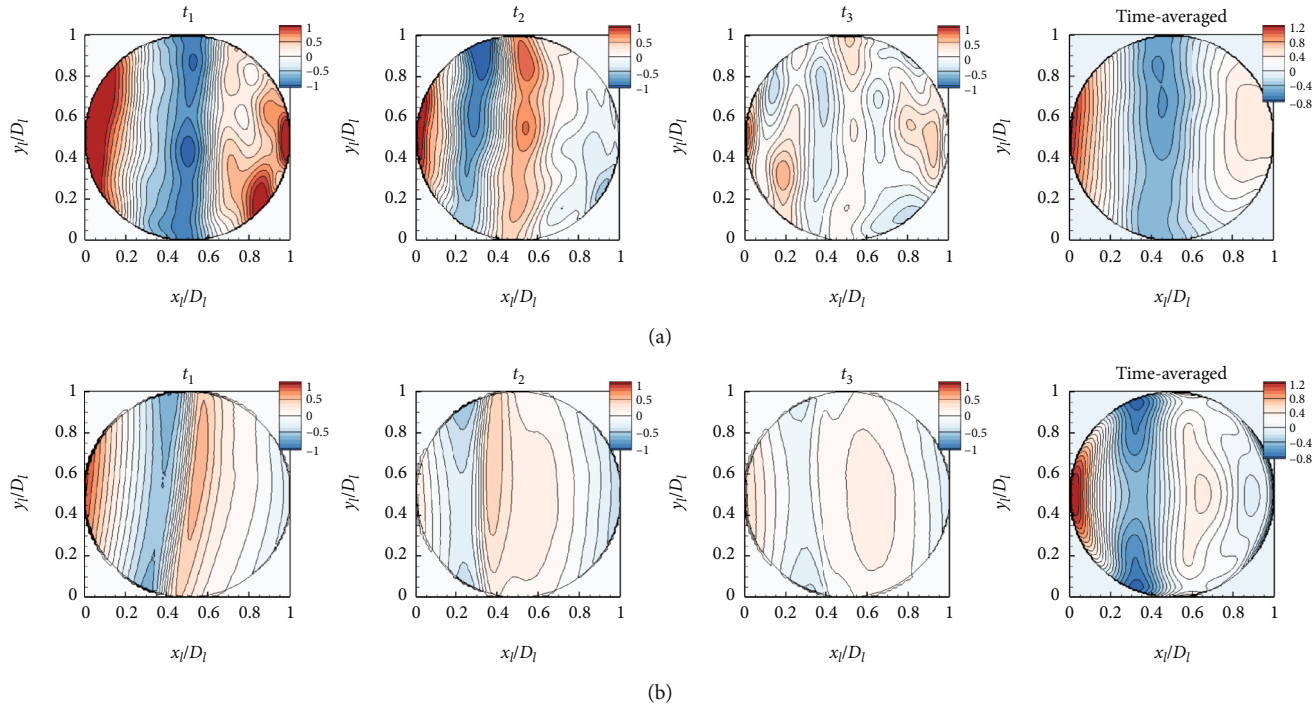

Figure 14: Transient wavefront distributions ($\mathrm{OPD}(x_l, y_l, t)$) and these time averages ($\langle \mathrm{OPD}(x_l, y_l) \rangle$): (a) experiment and (b) simulation.

there is a single peak frequency in the range of $St_D = 0.15 \sim 0.2$, and this frequency is dominated by the unsteady separation line and the separated recirculation region over the downstream portion of the turret [46]. Gordeyev and Jumper [1] have shown that there are three main flow modes in subsonic flow: (i) two counter-rotating trailing vortices separated from the top of the hemisphere of the turret; (ii) periodic alternating vortex shedding from the sides of the turret; (iii) two secondary vortices on either side of the turret base. In our numerical simulation, the monitored pressure in the separated shear layer has a single peak frequency of $St_D = 0.35$. That means, the frequency of the separation recirculation region is raised to $St_D = 0.35$. Due to the coupled dynamics of shock and separation, the shock has another inherent frequency, $St_D = 0.23$. It should also be emphasized that these two frequencies are sensitive to the freestream velocity. Here it is assumed that local shocks in transonic flow lead to further alienation of several flow modes and exhibit different frequencies. It requires further analysis.

4.1.1. Aero-Optical Effect. In this section, experimental measurements and simulation analysis of the aero-optical effects caused by the unsteady SBLI at the zenith of the turret are described.

Figure 14 shows the transient wavefront distributions $\mathrm{OPD}(x_l, y_l, t)$ obtained by experimental measurements and numerical simulations, as well as their time averages $\langle \mathrm{OPD}(x_l, y_l) \rangle$, all of which are dimensionless using the laser wavelength, λ=532 nm. A significant gradient in the transient wavefront corresponds to the local shock and separation line. It can be seen from the simulation and both individual experiments that as the shock oscillates back and forth, the significant gradient of the wavefront is also moving. Their time-averaged wavefront distributions are consistent, and the shocks and separation lines of both are located at the zenith of the turret, or $x_l/D_l = 0.5$. In front of the shock ($x_l/D_l < 0.4$), as air's velocity near the turret increases, its density decreases, and the corresponding index of refraction decreases, so the OPD decreases. In the separation zone after the shock ($x_l/D_l > 0.6$), the time-averaged values of pressure and density are unified, and the OPD fluctuations are mainly caused by turbulent fluctuation here. The root-mean-square of $\langle \mathrm{OPD}(x_l, y_l) \rangle$ obtained by the simulation and two experiments are 0.455 λ, 0.467 λ, and 0.447 λ. It means that the shock intensity of the simulation and the experiment are consistent. Further, the $\langle \mathrm{OPD}_{\mathrm{rms}} \rangle$ obtained by the simulation and two experiments are 0.498 λ, 0.593 λ, and 0.563 λ, respectively, and the relative error between them is 14%. It is probable due to the fact that there is more vortex information after the shock in the experimental flow, while the $\mathrm{OPD}(x_l, y_l, t)$ obtained by the simulation is smoother after the shock.

Figure 15 shows the root-mean-square of transient wavefront ($\mathrm{OPD}_{\mathrm{rms}}(t)$) and their PSD for the simulation and two experiments. The $\mathrm{OPD}_{\mathrm{rms}}$ and time moments corresponding to the transient wavefront distributions in Figure 14 are marked in Figure 15. The experimental results have rich high-frequency information, while the simulations are mainly large-scale features, which is the characteristic of the LES method. Both the experimental and simulated $\mathrm{OPD}_{\mathrm{rms}}$ have dual peak frequencies, including a concentrated peak frequency ($\mathrm{St}_D = 0.34$) and a broad peak frequency ($\mathrm{St}_D = 0.23 \sim 0.25$).

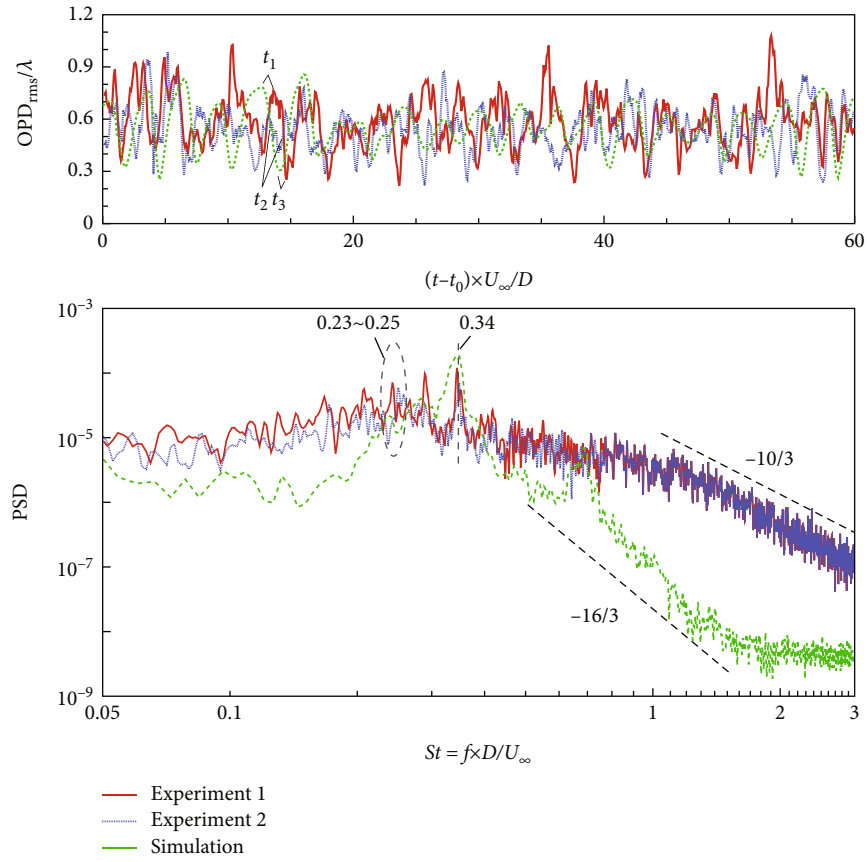

FIGURE 15: The root-mean-square of transient wavefront ($OPD_{rms}(t)$) and their PSD for experiment and simulation, where the solid red line and dotted blue line represent two experiments, and the green dotted line represents the simulation.

TABLE 3: Energy proportion of each POD mode for experiment and simulation.

	Mode	1	2	3	4	5	6	10	15	20
Experiment 1	Individual energy (%)	46.7	15.6	7.5	5.5	4.9	3.4	1.3	0.52	0.35
	Cumulative energy (%)	46.7	62.3	69.8	75.2	80.1	83.5	90.4	94.2	96.3
Experiment 2	Individual energy (%)	44.0	16.2	8.1	5.7	5.1	3.4	1.4	0.55	0.38
	Cumulative energy (%)	44.0	60.1	68.2	73.9	79.0	82.4	89.5	93.7	95.9
Simulation	Individual energy (%)	73.4	17.9	3.4	1.8	1.7	0.64	0.12	0.02	0.007
	Cumulative energy (%)	73.4	91.3	94.8	96.6	98.2	98.9	99.7	99.92	99.97

These two frequencies are consistent with the pressure characteristics in fluid dynamics, as shown in Figure 13. The PSD of OPD_{rms} obtained from the two experiments are coincident in the high-frequency part, and both satisfy the −10/3 law, while the simulated data decays faster (−14/3 law). It is mainly due to the high numerical dissipation of the LES method used in this paper. However, it does not affect the prediction of large-scale eddies and eigenfrequencies.

Table 3 lists the energy proportion of each POD mode for the simulation and two experiments. The energy proportions of each POD mode in the two experiments are the same, and these modal distributions are also the same, so Figure 16 only shows the POD mode of one experiment. For the experiment, the first two modes occupy 60% of the total energy, the first ten occupy 90%, and the first twenty occupy 96%. For the simulation, the first two modes occupy 91% of the total energy, and the first six occupy 99%, which means that the simulation results can reconstruct almost all spatiotemporal features using the six modes. The difference between the experimental and simulated energy ratios may be caused by the fact that the wind tunnel experiment has more interference information, while the numerical simulation only captures the main influencing factors.

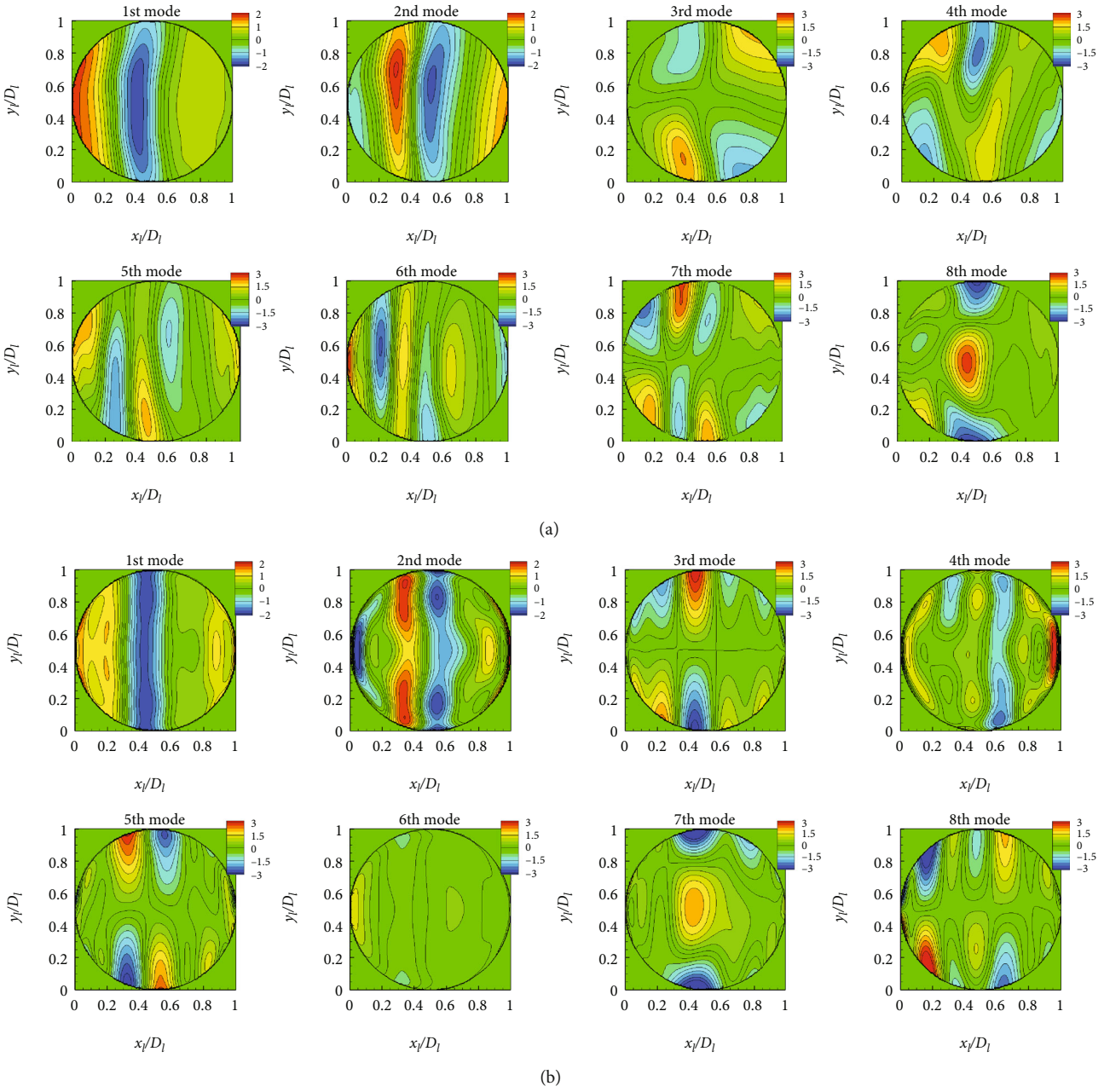

Figure 16: First eight POD mode distributions of wavefront, $\Phi_k(x_l, y_l)/\lambda$: (a) experiment and (b) simulation.

Figure 16 shows the distribution of the first eight POD modes for experiment and simulation. Figure 17 shows the coefficients of the first four POD modes over a time period of $60\,D/U_\infty$ and their PSDs. In Figure 16, the first two POD modes of the simulation and experiment are consistent, and both are symmetric about the spanwise. In Figure 17, the time coefficient a_1 of the first mode is approximately sinusoidal, while the time coefficient a_2 of the second mode is more complex than the sinusoidal shape. The time coefficients of the first two modes fluctuate with roughly the same period, and the difference between the two is 1/4 cycle. So the first two modes characterize the reciprocating shock motion. Further, the time coefficients of these two modes have apparent dual peak frequencies, while the time coefficients of other modes are absent. It indicates that the shock motion is the main reason for the dual-peak-frequency characteristics of the hydrodynamic and aero-optical effects. Considering that the first two POD modes cover more than half of the energy, the transient wavefront can be simplified as the superposition of the first mode and the second mode for application in some fields, such as transient adaptive correction.

In Figure 16, higher-order POD modes of experiment and simulation are different. The experiment's third, fourth,

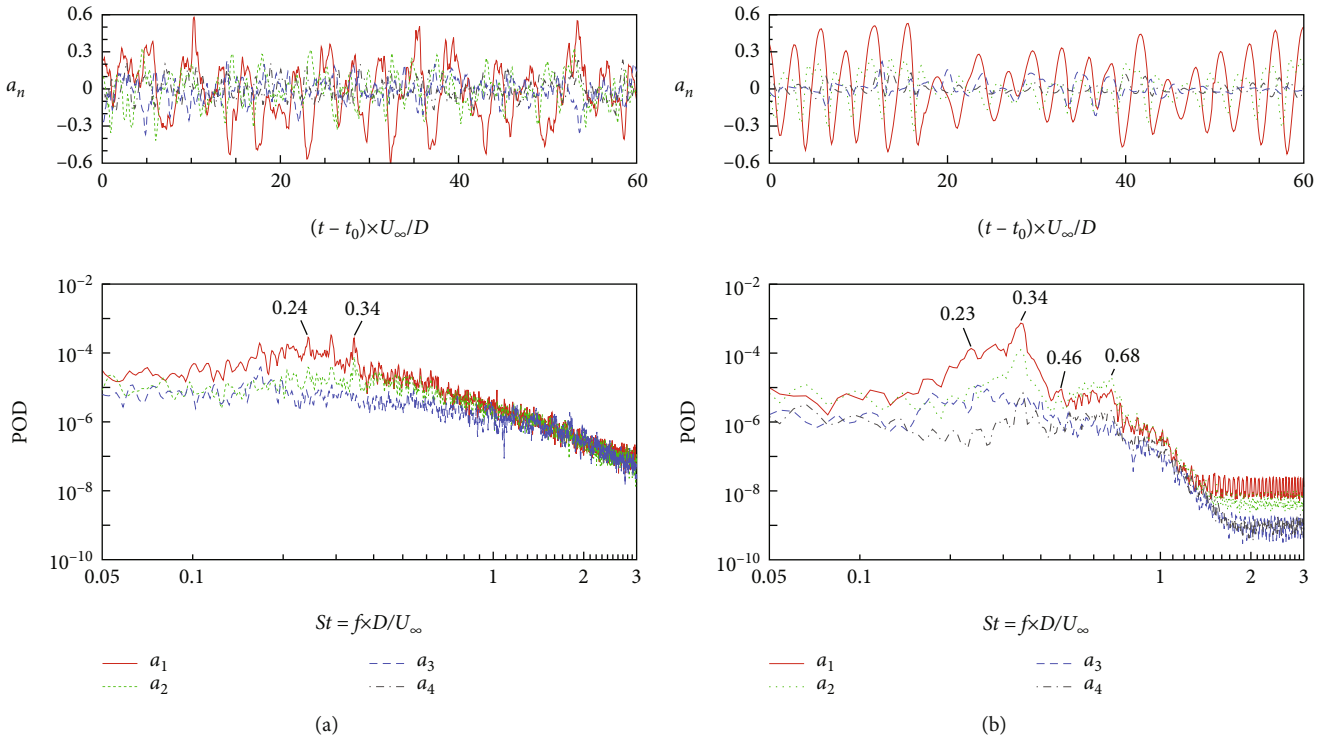

Figure 17: First four POD coefficients and their PSD: (a) experiment and (b) simulation.

and seventh modes are antisymmetric, which occupy 16% of the total energy. In contrast, the simulation's third, fifth, and eighth modes are antisymmetric, which only occupy 5%. The antisymmetric mode contains information about the spanwise motion of the transient wavefront, which means that the experimental data has more spanwise information. On the other hand, the experimental and simulated modalities share some similarities. For example, the peak- valley structure of the experimental seventh mode is similar to that of the simulated fifth mode. The experimental eighth mode and the simulated seventh are also similar.

5. Conclusions

Fluid dynamics and aero-optics of transonic flow (Ma = 0.7) over a hemisphere-on-cylinder turret, especially the characteristic unsteady excitation boundary layer interference, were tested in a wind tunnel using shadowing, Mach-Zehnder interferometer, and Shack-Hartmann wavefront measurements. The SST k-ω DES method and ray-tracing method are used to reproduce the transonic flow and optical aberration.

In fluid dynamics, numerical simulations reproduce the flow structures such as local shock, separated shear layer, turbulent wake, and necklace vortices in the transonic flow. The simulated flow structure mapped onto the bottom plate is consistent with the oil experiment. The time-averaged pressure distributions over the hemisphere are consistent for both experiment and simulation, and they both rise rapidly around 90° from the head due to SBLI. By monitoring the pressure here, the SBLI has multiple peak frequencies in the range of $St_D = fD/U_\infty = 0.23 \sim 0.35$.

In aero-optics, the wavefront at the zenith of the turret is around $0.56\,\lambda$~$0.59\,\lambda$, while the root-mean-square of the time-averaged wavefront is about $0.45\,\lambda$. The wavefront also has dual peak frequencies different from the single-peak-frequency phenomenon at small freestream velocities. The experimental wavefront power spectrum satisfies the −10/3 law, while the simulated result decay more rapidly due to the excessive viscous dissipation.

This paper also verifies that fast model decomposition of wavefront can be performed by combining Zernike decomposition and POD methods. The first ten modes of the experiment account for 90% of the total energy, while the first two modes of the simulation account for 91%. The first two modes of the experiment and simulation are consistent. They contain the reciprocating motion of the shock. The time coefficients for these two modes also have dual peak frequencies.

Data Availability

The data that support the findings of this study are available from the corresponding author upon reasonable request.

Conflicts of Interest

The authors declare that they have no known competing financial interests or personal relationships that could have appeared to influence the work reported in this article.

References

[1] S. Gordeyev and E. Jumper, "Fluid dynamics and aero-optics of turrets," *Progress in Aerospace Science*, vol. 46, no. 8, pp. 388–400, 2010.

[2] M. Wang, A. Mani, and S. Gordeyev, "Physics and computation of aero-optics," *Annual Review of Fluid Mechanics*, vol. 44, no. 1, pp. 299–321, 2012.

[3] K. G. Gilbert and L. J. Otten, *Aero-Optical Phenomena*, American Institute of Aeronautics and Astronautics, 1982.

[4] J. L. Moler and S. E. Lamberson, "Airborne laser (ABL) - A legacy and a future for high-energy lasers," in *Gas and Chemical Lasers and Intense Beam Applications*, vol. 3268, pp. 99–105, International Society for Optics and Photonics, 1998.

[5] G. P. Perram, M. A. Marciniak, and M. Goda, "High-energy laser weapons: technology overview. In: laser technologies for defense and security," *International Society for Optics and Photonics*, vol. 5414, pp. 1–25, 2004.

[6] S. Lamberson, H. Schall, and O. Alvarado, "Overview of airborne Laser's test program," in *2005 U.S. Air Force T&E Days*, American Institute of Aeronautics and Astronautics, 2005.

[7] E. J. Jumper and S. Gordeyev, "Physics and measurement of aero-optical effects: past and present," *Annual Review of Fluid Mechanics*, vol. 49, no. 1, pp. 419–441, 2017.

[8] H. Ding, S. Yi, Y. Xu, and X. Zhao, "Recent developments in the aero-optical effects of high-speed optical apertures: from transonic to high-supersonic flows," *Progress in Aerospace Science*, vol. 127, article 100763, 2021.

[9] G. W. Sutton, "Aero-optical foundations and applications," *AIAA Journal*, vol. 23, no. 10, pp. 1525–1537, 1985.

[10] E. J. Jumper and E. J. Fitzgerald, "Recent advances in aero-optics," *Progress in Aerospace Science*, vol. 37, no. 3, pp. 299–339, 2001.

[11] S. Abado, S. Gordeyev, and E. J. Jumper, "Two-dimensional high-bandwidth Shack-Hartmann wavefront sensor: design guidelines and evaluation testing," *Optical Engineering*, vol. 49, no. 6, article 064403, 2010.

[12] D. A. Buell, "Overview of 6-X 6-Foot Wind Tunnel Aero-Optics Tests," *Proceedings of the Aero-Optics Symposium on Electromagnetic Wave Propagation from Aircraft*, , , pp. 35–44, NASA Conference Publication, 1980.

[13] B. Vukasinovic, A. Glezer, S. Gordeyev, E. Jumper, and V. Kibens, "Active Control and Optical Diagnostics of the Flow Over a Hemispherical Turret," in *46th AIAA Aerospace Sciences Meeting and Exhibit*, p. 13, American Institute of Aeronautics and Astronautics, 2008.

[14] S. Gordeyev, M. L. Post, T. McLaughlin, J. Ceniceros, and E. J. Jumper, "Aero-optical environment around a conformal-window turret," *AIAA Journal*, vol. 45, no. 7, pp. 1514–1524, 2007.

[15] D. Nahrstedt, Y. C. Hsia, E. Jumper et al., "Wind tunnel validation of computational fluid dynamics-based aero-optics model," *Proceedings of the Institution of Mechanical Engineers, Part G: Journal of Aerospace Engineering*, vol. 223, no. 4, pp. 393–406, 2009.

[16] B. Vukasinovic, A. Glezer, S. Gordeyev, E. Jumper, and W. W. Bower, "Flow control for aero-optics application," *Experiments in Fluids*, vol. 54, no. 3, p. 1492, 2013.

[17] S. J. Beresh, J. F. Henfling, R. W. Spillers, and B. O. M. Pruett, "Unsteady shock motion in a transonic flow over a wall-mounted hemisphere," *AIAA Journal*, vol. 54, no. 11, pp. 3509–3515, 2016.

[18] N. D. Lucca, S. V. Gordeyev, and E. J. Jumper, "In-flight aero-optics of turrets," *Optical Engineering*, vol. 52, no. 7, article 071405, 2013.

[19] J. Morrida, S. Gordeyev, N. D. Lucca, and E. J. Jumper, "Shock-related effects on aero-optical environment for hemisphere-on-cylinder turrets at transonic speeds," *Applied Optics*, vol. 56, no. 16, pp. 4814–4824, 2017.

[20] M. D. White, "High-order parabolic beam approximation for aero-optics," *Journal of Computational Physics*, vol. 229, no. 15, pp. 5465–5485, 2010.

[21] A. Mani, M. Wang, and P. Moin, "Resolution requirements for aero-optical simulations," *Journal of Computational Physics*, vol. 227, no. 21, pp. 9008–9020, 2008.

[22] E. Mathews, E. Mathews, K. Wang, K. Wang, M. Wang, and E. J. Jumper, "Turbulence scale effects and resolution requirements in aero-optics," *Applied Optics*, vol. 60, no. 15, pp. 4426–4433, 2021.

[23] J. E. Pond and G. W. Sutton, "Aero-optic performance of an aircraft forward-facing optical turret," *Journal of aircraft*, vol. 43, no. 3, pp. 600–607, 2006.

[24] J. Ladd, M. Mani, and W. Bower, "Validation of aerodynamic and optical computations for the unsteady flow field about a hemisphere-on-cylinder turret," in *27th AIAA Applied Aerodynamics Conference. Fluid Dynamics and Co-Located Conferences*, American Institute of Aeronautics and Astronautics, 2009.

[25] P. E. Morgan and M. R. Visbal, "Hybrid Reynolds-averaged Navier-stokes/large-Eddy simulation investigating control of flow over a turret," *Journal of Aircraft*, vol. 49, no. 6, pp. 1700–1717, 2012.

[26] R. Jelic, S. Sherer, and R. Greendyke, "Simulation of various turrets at subsonic and transonic flight conditions using OVERFLOW," *Journal of Aircraft*, vol. 50, no. 2, pp. 398–409, 2013.

[27] W. J. Coirier, M. Whiteley, D. J. Goorskey et al., "Aero-optical evaluation of notional turrets in subsonic, transonic and supersonic regimes," in *45th AIAA Plasmadynamics and Lasers Conference*, American Institute of Aeronautics and Astronautics, 2014.

[28] E. R. Mathews, K. Wang, M. Wang, and E. J. Jumper, "LES of an aero-optical turret flow at high Reynolds number," in *54th AIAA Aerospace Sciences Meeting*, American Institute of Aeronautics and Astronautics, 2016.

[29] Y. Zhou, Y. Zhao, and Y. Zhao, "A study on the separation length of shock wave/turbulent boundary layer interaction," *International Journal of Aerospace Engineering.*, vol. 2019, article 8323787, pp. 1–10, 2019.

[30] C. M. Wyckham and A. J. Smits, "Aero-optic distortion in transonic and hypersonic turbulent boundary layers," *AIAA Journal*, vol. 47, no. 9, pp. 2158–2168, 2009.

[31] B. C. Platt and R. Shack, "History and principles of Shack-Hartmann wavefront sensing," *Journal of Refractive Surgery*, vol. 17, no. 5, pp. S573–S577, 2001.

[32] F. R. Menter, M. Kuntz, and R. Langtry, "Ten years of industrial experience with the SST turbulence model," *Turbulence, heat and mass transfer*, vol. 4, pp. 625–632, 2003.

[33] D. B. Spalding, "A single formula for the "law of the wall."," *Journal of Applied Mechanics*, vol. 28, no. 3, pp. 455–458, 1961.

[34] W. C. Gardiner, Y. Hidaka, and T. Tanzawa, "Refractivity of combustion gases," *Combustion and Flame*, vol. 40, pp. 213–219, 1981.

[35] R. Tyson, *Principles of Adaptive Optics*, CRC Press, 3rd ed. edition, 2010.

[36] P. E. Cassady, S. F. Birch, and P. J. Terry, "Aero-optical analysis of compressible flow over an open cavity," *AIAA Journal*, vol. 27, no. 6, pp. 758–762, 1989.

[37] K. Taira, S. L. Brunton, S. T. M. Dawson et al., "Modal analysis of fluid flows: an overview," *AIAA Journal*, vol. 55, no. 12, pp. 4013–4041, 2017.

[38] B. Malouin, J. Y. Trépanier, and M. Gariépy, "Interpolation of transonic flows using a proper orthogonal decomposition method," *International Journal of Aerospace Engineering*, vol. 2013, Article ID 928904, 11 pages, 2013.

[39] V. Lakshminarayanan and A. Fleck, "Zernike polynomials: a guide," *Journal of Modern Optics*, vol. 58, no. 7, pp. 545–561, 2011.

[40] A. Mani, M. Wang, and P. Moin, "Computational study of optical distortions by separated shear layers and turbulent wakes," *Journal of Fluid Mechanics*, vol. 625, pp. 273–298, 2009.

[41] E. R. Mathews Jr., *Numerical and Theoretical Analysis of Aero-Optics with Application to an Optical Turret*, University of Notre Dame, 2017.

[42] J. J. Morrida, S. Gordeyev, and E. J. Jumper, "Transonic Flow Dynamics Over a Hemisphere in Flight," in *54th AIAA Aerospace Sciences Meeting*, p. 1349, American Institute of Aeronautics and Astronautics, 2016.

[43] S. Gordeyev, T. E. Hayden, and E. J. Jumper, "Aero-optical and flow measurements over a flat-windowed turret," *AIAA Journal*, vol. 45, no. 2, pp. 347–357, 2007.

[44] B. Vukasinovic, D. Brzozowski, and A. Glezer, "Fluidic control of separation over a hemispherical turret," *AIAA Journal*, vol. 47, no. 9, pp. 2212–2222, 2009.

[45] J. Morrida, S. Gordeyev, N. D. Lucca, and E. J. Jumper, "Aero-optical investigation of transonic flow features and shock dynamics on hemisphere-on-cylinder turrets," in *53rd AIAA Aerospace Sciences Meeting*, American Institute of Aeronautics and Astronautics, 2015.

[46] S. Gordeyev, N. De Lucca, E. J. Jumper et al., "Comparison of unsteady pressure fields on turrets with different surface features using pressure-sensitive paint," *Experiments in Fluids*, vol. 55, no. 1, p. 1661, 2014.